Two-Dimensional Copper Tetrahydroxyquinone Conductive Metal Organic Framework for Selective CO_2 Electrocatalysis at Low Overpotentials

Leily Majidi[1], Alireza Ahmadiparidari[1], Nannan Shan[2], Saurabh N. Misal[1], Khagesh Kumar[3], Zhehao Huang[4], Sina Rastegar[1], Zahra Hemmat[1], Xiaodong Zou[4], Peter Zapol[2], Jordi Cabana[3], Larry A. Curtiss[2&], Amin Salehi-Khojin[1&]

[1] Department of Mechanical and Industrial Engineering, University of Illinois at Chicago, Chicago, IL, 60607, USA.
[2] Materials Science Division, Argonne National Laboratory, Argonne, IL 60439, USA.
[3] Department of Chemistry, University of Illinois at Chicago, Chicago, IL, 60607, USA.
[4] Department of Materials and Environmental Chemistry, Stockholm University, Stockholm, 10691, Sweden.

[&]Corresponding authors: salehikh@uic.edu, curtiss@anl.gov

Metal organic frameworks (MOFs) are promising materials for electrocatalysis, however, lack of electrical conductivity in the majority of existing MOFs limits their effective utilization in the field. Herein, we report an excellent catalytic activity of a two-dimensional copper (Cu)-based conductive MOF, copper tetrahydroxyquinone (Cu-THQ), for aqueous CO_2 reduction reaction at low overpotentials. It is revealed that Cu-THQ nanoflakes (NFs) with an average lateral size of 140 nm exhibit a negligible overpotential of 16 mV for the activation of this reaction, a high current density of ~173 mA cm^{-2} at -0.45 V vs RHE, an average Faradaic efficiency of ~91% towards CO production and a remarkable turnover frequency as high as ~20.82 s^{-1}. In the low overpotential range, the obtained CO formation current density is more than 35 and 25 times higher compared to state-of-the-art MOF and MOF-derived catalysts, respectively. Our *operando* Cu K-edge X-ray absorption near edge spectroscopy and density functional theory calculations reveal the existence of reduced Cu (Cu^+) during CO_2RR which reversibly returns to Cu^{2+} after the reaction. The outstanding CO_2 catalytic functionality of c-MOFs could open a way towards high-energy-density electrochemical systems.

Growing worldwide energy demand and rising consumption rate of fossil fuels could lead to catastrophic consequences facing modern society. To conquer the upcoming energy crisis and to develop sustainable energy technologies, discovery of new materials with outstanding functionalities is necessary. In this regard, metal organic frameworks (MOFs) are ideal materials due to their extraordinary structural versatility, synthetic tunability, ultrahigh porosity, and high surface area[1–6]. MOFs are crystalline structures composed of inorganic metal ions and organic ligands that can be synthesized through a bottom-up assembly approach under solvothermal conditions. To date, numerous MOFs are used extensively for bulk applications such as heterogeneous catalysis, gaseous energy storage (H_2 and CH_4), and CO_2 capture, separations and reduction reaction[7–13]. However, the insulating nature (lack of electrical conductivity) of the majority of the existing MOFs restricts their successful utilization in electrocatalysis which is central to applications in the field of energy storage and generation[14,15]. In order to mitigate this challenge, molecular engineering strategies have been recently employed to harness the reticular chemistry and robust tunability of classical MOFs to develop conductive MOFs (c-MOFs) which demonstrate both porosity and electrical conductivity[14–17]. While the c-MOFs have recently shown a great promise in hydrogen evolution reaction (HER)[18,19], oxygen reduction and evolution reaction[15,19,20] and supercapacitors[21,22], there still remains a lack of highly efficient c-MOF-based catalysts to be utilized in core electrochemical reactions such as electrochemical CO_2 reduction reaction (CO_2RR).

Herein, we report the CO_2RR electrocatalytic activity of a two-dimensional (2D) copper (Cu)-based c-MOF, copper tetrahydroxyquinone (Cu-THQ) at low overpotentials using a hybrid electrolyte comprising of 1 M choline chloride and 1 M potassium hydroxide (KOH). This hybrid electrolyte was selected due to its superior ionic conductivity, high CO_2 solubility and stability for the CO_2RR[23]. The bulk Cu-THQ with the chemical formula of $Cu_3(C_6O_6)_2$ and electrical conductivity of ~1.5×10^{-7} S cm^{-1} was synthesized based on a method previously reported (see Supplementary Information S1 and Ref 17), and exfoliated into 2D nanoflakes (NFs) via liquid-phase exfoliation technique for an increased surface to volume ratio (see Supporting Information S2). The successful synthesis of 2D structures was confirmed by our comprehensive characterization study, including energy dispersive X-ray spectroscopy (EDX), high-resolution transmission electron microscopy (HRTEM), X-ray photoelectron spectroscopy (XPS) and atomic force microscopy (AFM). Moreover, operando Cu K-edge X-ray absorption near edge

spectroscopy and density functional theory calculations shed light on identifying the active sites and chemical changes during the CO_2RR.

Figure 1a shows the dispersed NFs of Cu-THQ in isopropyl alcohol (IPA) with a distinct color after liquid-phase exfoliation (see Experimental Section). A typical atomic force microscopy (AFM) image of Cu-THQ NFs deposited on Si/SiO_2 substrate is shown in Figure 1b. The statistical thickness analysis of 40 randomly selected flakes revealed an average thickness of 10.1 +/- 6.7 nm (Figure 1c). Figure 1d shows an average lateral size of 140 +/- 52 nm for one batch of Cu-THQ NFs obtained by dynamic light scattering (DLS) (see Supporting Information S3 for the rest of DLS and AFM results). To examine the structural stability of c-MOF NFs after exfoliation, high-resolution transmission electron microscopy (HRTEM) images were obtained. The HRTEM images (Figure 1e-g) clearly show elliptical pores, smaller than 1 nm with a honeycomb arrangement along [001] with d_{110} = 11.7 Å and d_{020} = 11.0 Å, which corresponds well with the AB stacking model of Cu-THQ (calculated d_{110} = 11.2 Å and d_{020} = 10.9 Å)[17]. Elemental mapping with energy-dispersive spectroscopy (EDS) indicates a homogeneous C, O and Cu distribution in the exfoliated Cu-THQ sample (see Figure S3). These observations confirm that the crystal structure was well preserved in exfoliated Cu-THQ samples. X-ray Photoelectron spectroscopy (XPS) was also performed on the bulk and exfoliated Cu-THQ sample deposited on gas diffusion electrodes (GDE). Full energy spectra results shown in Figure 1h indicates the presence of Cu, C and O species for both bulk and 2D Cu-THQ NFs (see Supporting Information section S5). Moreover, a small amount of N species is observed in the XPS spectra due to the synthesis process[17]. An extra F peak is also observed in the XPS survey spectrum of the Cu-THQ NFs which is due to the polytetrafluoroethylene (PTFE) present on the GDE substrate[24]. Overall, our characterization results confirm the structural integrity of c-MOF after exfoliation.

To evaluate the catalytic performance of 2D c-MOF, linear sweep voltammetry (LSV) experiments were performed for different particle sizes. The LSV experiments were carried out in a three-electrode setup containing CO_2 saturated 1 M choline chloride and 1 M KOH at a scan rate of 50 mV s^{-1}[23]. To prepare the working electrodes, the synthesized c-MOF NFs were deposited on GDE substrates (see Experimental Section). $Ag/AgNO_3$ and Pt mesh were used as reference and counter electrodes, respectively (see Supporting Information S6-7). The LSV results shown in Figure 2a indicate that Cu-THQ NFs with the average particle size of 140 nm delivered the highest current

density of ~173 mA cm^{-2} at -0.45 V vs RHE. At the same potential, the current densities for average particle sizes of 300 nm and 600 nm are ~146.3 mA cm^{-2} and ~96 mA cm^{-2}, respectively.

To detect the gas products and measure the onset potentials of the corresponding reactions, LSV experiments were performed in a two-compartment cell at a low scan rate of 1 mV s^{-1} with real time product analysis using differential electrochemical mass spectroscopy (DEMS) (Figure 2b). During the DEMS online measurement, CO was observed as a major product and no other carbon-based gas phase products were detected. We obtained an onset potential of -0.126 V vs RHE for CO formation, suggesting a low overpotential of 16 mV compared to the thermodynamic potential of -0.11 V for this reaction[25] (see Supporting Information S8-9). This value is so far the lowest onset potential reported for CO_2RR compared to the state-of-the-art catalysts[25–33] (also see Table S2). With the overpotential continuously increasing, CO production faced an increase in the tested potential range. H_2 production was also negligible and remained stable during the experiment.

To gain more insight into the gas product formation during CO_2RR, one-hour chronoamperometry experiments were performed at three different potentials in the range of -0.135 and -0.43 V vs RHE. Current density profiles for these experiments show no more than 20% decrease compared to the current densities observed in LSV experiment which is attributed to the charging current (capacitive behavior) in the LSV measurements (see Figure S8). DEMS was also used in each experiment to detect the gas products. Similar to the LSV experiment, no carbon-based gas products were observed other than CO (see the DEMS results in Figure S9). The corresponding Faradaic efficiency (F.E.) of CO and H_2, as depicted in the inset of Figure 2b, is on average ~91% at the potential window from -0.135 V to -0.43 V vs RHE. Furthermore, the average F.E. for H_2 formation was measured to be negligible (< 1%) in this potential window. The remaining F.E. is attributed to the loss in the system and/or small percentage of possible liquid products. These results indicate that CO_2RR with Cu-THQ NFs is favorable towards CO production in the -0.135 V to -0.43 V vs RHE range.

The achieved current density with Cu-THQ NFs (Figure 2a) is the highest value ever reported for the MOF and MOF-derived catalysts in CO_2RR, especially with selectivity towards CO formation (see Table S2) [34–42]. In particular, the CO formation current density achieved by Cu-THQ NFs at -0.43 V vs RHE is ~25 times higher than that of bimetallic Co/Zn zeolitic imidazolate framework-derived Co-N_2 at the potential of -0.48 V vs RHE[38] and ~37 times higher than the value reported

for porphyrin-based MOF of PCN-222(Fe)/C at -0.45 V vs RHE[42]. In addition, Table S3 compares the electrochemical performance of Cu-THQ NFs with a number of Cu-based catalysts with CO production. For instance, the CO formation current density obtained by Cu-THQ NFs at -0.43 V vs RHE is approximately 38 and 35 times higher than the values achieved by the state-of-the-art Cu based catalysts of Cu/$Ni(OH)_2$ nanosheets at -0.5 V vs RHE[43] and annealed Cu foam at -0.45 V vs RHE[44], respectively. Moreover, Cu-THQ NFs greatly outperform noble metal (e.g., Ag, Au)[25,30–33] and other non-precious catalysts[26–29].

Density functional theory (DFT) calculations revealed that Cu species together with neighboring O species in the catalyst are the active sites contributing to the CO_2RR (see the DFT discussion below). Therefore, to determine the turnover numbers (TON) of CO production per mole of Cu, we measured the total Cu loading on the cathode using inductively coupled plasma optical emission absorption spectroscopy (ICP-OES, see Supporting Information S13). Our experiments revealed that approximately 1.6×10^{-7} moles of Cu exist per square centimeter of the cathode electrode. The TON values of CO production were then calculated from chronoamperometry experiments assuming that all Cu species in the catalyst are electrochemically active (see Supporting Information S14). Figure 2c shows an increasing trend of TON values with the applied potentials where at the potential of -0.43 V vs RHE an exceptionally high value of $\sim 7.49 \times 10^4$ was obtained after one hour. CO formation turnover frequency (TOF) was also found to be ~20.82 s^{-1} at -0.43 V vs RHE (inset of Figure 2c), which is by far the highest TOF reported for CO_2RR in low overpotential range (see Table S1)[26–30,32,33,45,46].

The stability of Cu-THQ catalyst was investigated using XPS experiments over an extended 7-hour chronoamperometry experiment at the controlled potential of -0.43 V vs. RHE (see Supporting Figure S10). Figure 2d shows the Cu 2p spectra of Cu-THQ cathode before and after the electrochemical reaction. The results indicate that before the reaction, the Cu-THQ is composed of Cu^{2+}. After the CO_2RR, the two Cu^{2+} main peaks in the pristine cathode located at ~934.9 eV and ~954.8 eV were shifted to lower binding energies of 933.7 eV and 953.6 eV, respectively. The binding energies of both pristine and cycled samples were within the range reported in the NIST database for a formal oxidation state of Cu^{2+}[47]. While the pristine state is closer to reported values for Cu^{2+}-O^{2-} bonds in compounds like hydroxides and carbonates in the literature[48,49], the cycled state is more consistent with Cu^{2+}-O^{2-} bonds in oxides[50–52]. However, metallic Cu and Cu^{+}-O^{2-} species are typically observed at least 1 eV lower in energy than any

signals observed here[47,50]. Therefore, the peak shift observed after cycling does not signify reduction, but can rather be attributed to a change in the chemical environment of Cu^{2+} after electrocatalysis[51]. Furthermore, the two Cu^{2+} satellite peaks observed in the pristine cathode faced a significant decrease in intensity due to the reduction reaction, but they remained after cycling. The obtained results confirmed the stability of catalyst and were consistent with the XPS results after 7-hour chronoamperometry. Moreover, ex-situ Cu L_3-edge X-ray absorption spectroscopy (XAS) experiments were performed on the pristine state and after cycling for 1 and 7 hours, respectively (Figure 2e). The Cu L_3-edge spectrum results from the dipole allowed transition of Cu $2p_{3/2}$ electrons into empty Cu 3d-O 2p hybridized states, if present, with a weaker transition allowed to Cu 4s-O 2p states at higher energy. The pristine Cu-THQ NFs show a sharp peak at 930.85 eV, with weaker signals at 934.1 eV and 937.9 eV which are broadly consistent with reported peak positions of a formal Cu^{2+} state[53]. The peak around 931 eV arises from the $2p_{3/2}$-> $3d^9$ transition[53], which is absent in Cu^+ and Cu^0 because they both have a filled *d* shell; both have peaks near 933.7 eV, absent in our data[54]. After the reaction, the most intense peak shifts to lower energy, by 0.2-0.3 eV. The persistence of this $2p_{3/2}$-> $3d^9$ transition again supports a dominant formal Cu^{2+} state, with absence of any obvious signals indicating concurrent presence Cu^+ and Cu^0. The slight shift to lower energy with higher reaction time suggests a change in the chemical environment of Cu^{2+} as a result of catalysis, in agreement with the XPS results. The position of the Cu^{2+} L_3-edge peaks is known to be very sensitive to the nature of its covalent interaction with different ligands[55].

Additionally, a long-term chronoamperomtery experiment (24 hours) was performed for Cu-THQ NFs at the potential of -0.43 V vs. RHE and the stability of catalyst was further confirmed via XPS (see Supporting Figures S11 and S12). Moreover, nuclear magnetic resonance (NMR) spectroscopy was utilized to evaluate the stability of the electrolyte. The obtained ^1H and ^{13}C NMR spectra confirm the stability of the choline chloride/KOH electrolyte after the long-term chronoamperometry experiment (see Supporting Information Section S12).

To get insight into the electronic and chemical changes during the CO_2RR, *operando* Cu K-edge X-ray absorption near edge spectroscopy (XANES) was performed (Figure 2F). The spectra are the result of an electron transition from the occupied 1s to the unoccupied 4p bands and, subsequently, the continuum upon excitation by high energy X-ray radiation[56]. Figure 2F shows Cu K-edge XANES spectra for the Cu-THQ at open circuit voltage (OCV), -0.43 V vs RHE, and

12 minutes after the reaction was stopped and the electrode was returned to OCV. The XANES spectrum of the material at OCV shows an edge feature at ~8986 eV, associated with a Cu 1s→4p and ligand-to-metal charge transfer shakedown[57], and a broad white line peak around 8995 eV. These features confirm the Cu^{2+} state in the pristine compound, consistent with the reference spectrum of CuO and other reports in the literature[56]. When a cathodic potential was applied, a broad feature developed, centered around 8980.5 eV, but spanning well into the onset of the absorption edge at ~8985 eV. The position of the edge also shifted to lower energy with respect to the pristine state. These changes suggest the reduction of Cu^{2+}. Recent studies of CO_2 electrocatalysis with Cu^{2+} have reported the reduction to metallic Cu during the reaction[58,59]. In this case, because both Cu^{+} and Cu^{0} show features between 8980 and 8983 eV (see reference spectra for Cu_2O and metallic Cu in Figure 2F)[59], it cannot be discarded that both states are present under catalysis. Indeed, a separate experiment with three recorded scans where the potential was held at -0.43 V vs RHE for 20 min per scan, showed an evolution of a peak at 8983 eV that is clearly characteristic of Cu^{+} (see Supporting Figure S14(b)). It is possible that the 2-electron reduction of Cu^{2+} occurs in single-electron steps that are very close in potential, inducing co-existence in the conditions of CO_2RR. Further studies are needed to clarify this fact. After collecting data at -0.43 V vs RHE, the cell was returned to open circuit to collect XANES of the relaxed catalyst. The corresponding spectrum was again consistent with a formal Cu^{2+} state, but there were subtle differences in line shape with respect to the pristine compound, consistent with both *ex situ* XPS and XAS at the Cu L_3-edge. These observations indicate a very rapid return to an oxidized state, but with differences in the chemical environment of Cu, changing bonding with ligands. They are also subtly, but importantly different from the observations of re-oxidation of metallic Cu by Karapinar *et al.*[58] and Weng *et al.*[59] who exposed the reduced electrode either to air for 10 h or to oxidizing potentials, compared to the short relaxation in the electrolyte, at OCV, carried out here. Assuming that some metallic Cu formed during CO_2RR, the fact that the catalyst returned to Cu^{2+} in a short time would imply the formation of very small Cu clusters that would require a significantly lower reduction potential compared to the bulk. In fact, Karapinar *et al.* reported virtually no re-oxidation during OCV of the 0.5-nm clusters of metallic Cu formed during CO_2RR, with prolonged air exposure needed for the process to occur [58].

DFT calculations were performed to study activity, selectivity and stability of Cu-THQ (see Supporting Information S17 for details). The reaction mechanism adopted for CO formation from

CO_2 is given in Equations (1-3). The intermediate CHO* formation is also included for comparison of competing pathways, as shown in Equation (4). The other competing pathways involving various intermediates are illustrated in Figure S16. The asterisk indicates species adsorbed on the surface.

$$CO_2(g) + H^+ + e^- \rightarrow COOH^* \quad (1)$$

$$COOH^* + H^+ + e^- \rightarrow CO^* + H_2O(l) \quad (2)$$

$$CO^* \rightarrow CO(g) + * \quad (3)$$

$$CO^* + H^+ + e^- \rightarrow CHO^* \quad (4)$$

The structures of clean Cu-THQ surface and the key intermediates are shown in Figure 3a, b, and c. In CO_2 reduction, the first proton-electron transfer gives COOH on Cu-THQ surface (see Equation (1)). The COOH binds on O site next to Cu atom via unsaturated C, as shown in Figure 3b. The second proton-electron transfer yields CO and water, as described in Equation (2). The CO binds on Cu site via C atom with the perpendicular configuration (as depicted in Figure 3c). Due to the CO adsorption, the Cu atom is pulled out of plane as shown in the side view in the bottom panel in Figure 3c.

The free energy diagrams along with solvation correction, ΔG_{sol}, were generated using the energies of a Cu-THQ clean surface, CO_2 gas and a proton-electron pair as the references. As shown in Figure 3d, the reaction of COOH* formation at 0 V vs RHE (i.e. dotted blue lines) is endergonic with a free energy of 0.60 eV. Compared to COOH* formation, the second proton-electron pair transfer to form CO* and H_2O at 0 V vs. RHE is more facile with ΔG_{sol} of -0.88 eV. CO desorption from the surface requires 0.90 eV. Therefore, the first proton-electron transfer step to form COOH* is considered as the potential limiting step for CO evolution with the limiting potential of 0.60 V vs RHE. Since the equilibrium potential is 0.31 V vs RHE based on DFT calculations for CO formation, the overpotential of -0.29 V is needed in order to make the reaction proceed downhill as shown with solid blue lines in Figure 3d.

It is well known that metallic Cu is able to selectively catalyze CO_2 to hydrocarbons[60–62]. With this in mind, we computed the free energies of CHO* formation on Cu-THQ (see Equation (4)), which is commonly considered as the potential limiting step for methane and methanol production on Cu (211) surface[60]. At 0 V vs. RHE, the CHO* formation on Cu-THQ from CO* demands a ΔG_{sol} of 0.74 eV as shown with dotted red lines in Figure 3d, indicating that the reaction is still unfavorable, even at applied overpotential of η of -0.29 V (see solid red lines in Figure 3d). It is noted that although the CHO* formation (ΔG_{sol} =0.74 eV) is less positive than CO desorption (0.90 eV), the CO adsorption free energies decrease as the adsorption coverage increases, as displayed in Figure 3e. Therefore, CO* formation is competing for the surface Cu sites with CHO* formation. However, as the overpotential becomes more negative, CHO* production is expected to become more favorable (see reaction pathway at -0.29V in Figure 3d), which will lead to a decreased CO production at higher potentials as compared to other products. It is believed that C_{2+} products selectivity from CO_2 reduction remains low on Cu based catalyst because it requires high over potential for the intermediates of C-C coupling. Therefore, we did not include the pathways for C_{2+} products formation on Cu-THQ. (Nature Catalysis 2020, 3, 478–487, Nature Catalysis, 2019, 2, 198–210) To investigate stability of Cu-THQ under CO_2RR conditions, we have evaluated thermodynamics of two-electron Cu reduction to bulk Cu metal as shown in Figure S17. We conclude on the basis of our DFT calculations that if Cu in the Cu-THQ is reduced to relatively large Cu particles, it is unfavorable thermodynamically to oxidize Cu back into the original Cu-THQ structure.

To have a closer look into the change in the charge of Cu sites before and during the CO_2RR reaction, the Bader charge analysis was performed[63–65]. The calculated charges of Cu atoms in Cu_2O (0.55e) and CuO (0.95e) bulk structures were used as references. The charges of Cu, O and C atoms on a clean Cu-THQ surface and on the Cu-THQ surface with adsorbed CO, i.e. CO*, are labeled in Figure 3a and c, respectively. The Cu atom on the clean surface is identified as divalent copper as it holds a positive Bader charge of 1.03e. After CO adsorption on this Cu site, Cu becomes less positive, corresponding to an intermediate between a monovalent and divalent reference. Analysis of charge distribution indicates an electron transfer from C to Cu upon CO adsorption (see charge values in Figure 3c). This observation would support the existence of reduced Cu from the *operando* XANES measurements and point toward the active role of Cu^+ during CO_2RR.

In summary, we found that c-MOFs are ideal catalytic candidates to drastically enhance the energy efficiency and product selectivity of CO_2RR. In particular, we revealed that 2D Cu-THQ c-MOF delivers record values of TOFs and TONs for CO formation at low overpotentials and exhibits a negligible overpotential for CO_2 reduction reaction. XANES and DFT results further supported the electrochemical results and provided more in-depth insight on the reaction mechanism. These interesting findings can open a new way for further advances in core electrocatalytic reactions with applications in energy storage and conversion systems.

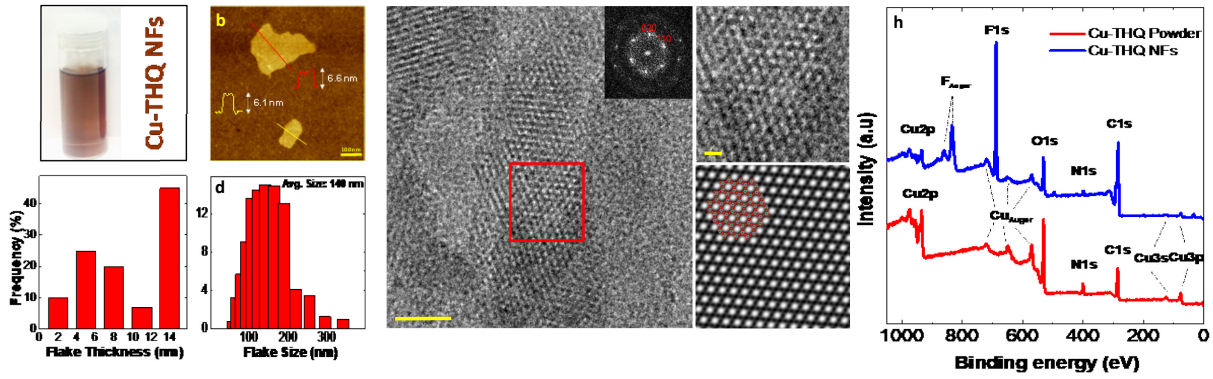

Figure 1. Characterization of 2D c-MOF NFs. (**a**) Cu-THQ NFs dispersed in IPA (**b**) Representative AFM image of Cu-THQ NFs. (**c**) Thickness distribution of Cu-THQ NFs. (**d**) Lateral size distribution of Cu-THQ NFs. (**e**) HRTEM images of Cu-THQ NFs along [001] showing an elliptical pore packing. The inset is the Fourier transform of the image. (**f**) HRTEM image in the red box in (E). (**g**) Lattice-averaged and symmetry-imposed image obtained from the HRTEM image in (F). Embedded is the AB stacking model of Cu-THQ. (**h**) XPS survey spectra of Cu-THQ powder and NFs.

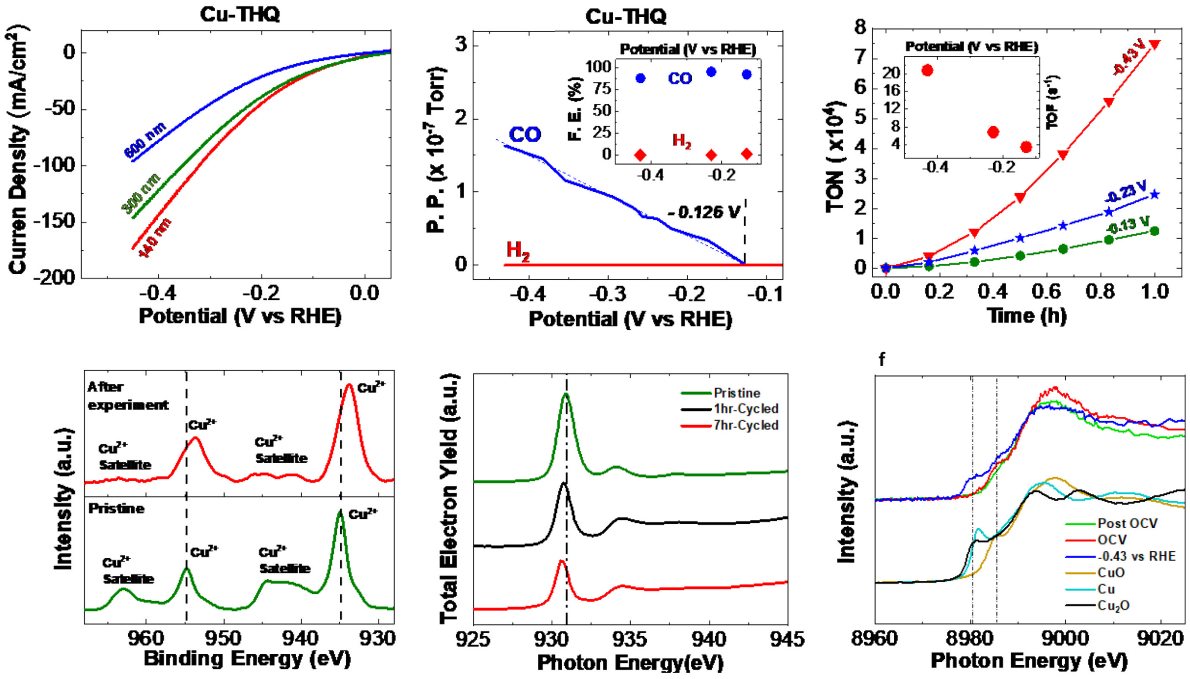

Figure 2. CO_2 reduction performance at low overpotentials, product analysis, and electronic and chemical characterization of Cu-THQ catalyst. (**a**) LSV results (scan rate of 50 mV s^{-1}) for electrochemical reduction of CO_2 in 1 M choline chloride and 1 M KOH using Cu-THQ NFs for different particle sizes. (**b**) DEMS analysis results for CO and H_2 production during LSV experiment (scan rate of 1 mVs^{-1}) for Cu-THQ NFs. Blue dotted line shows fitted

line for increase in CO from -0.126 V to -0.43 V vs RHE. The inset shows Faradaic efficiencies of CO and H_2 formation for different potentials. (**c**) TONs for CO production during 1-hour chronoamperometry experiments at controlled potentials. The inset shows TOFs at these potentials after 1 hour. (**d**) XPS results of Cu 2p region in Cu-THQ catalyst before and after 7-hour CO_2RR experiment at -0.43 V vs RHE. (**e**) Cu-L_3 XAS results of Cu-THQ catalyst before and after 7-hour CO_2RR experiments shown in total electron yield mode. (**f**) Operando XANES results of Cu-THQ catalyst recorded at Cu K-edge.

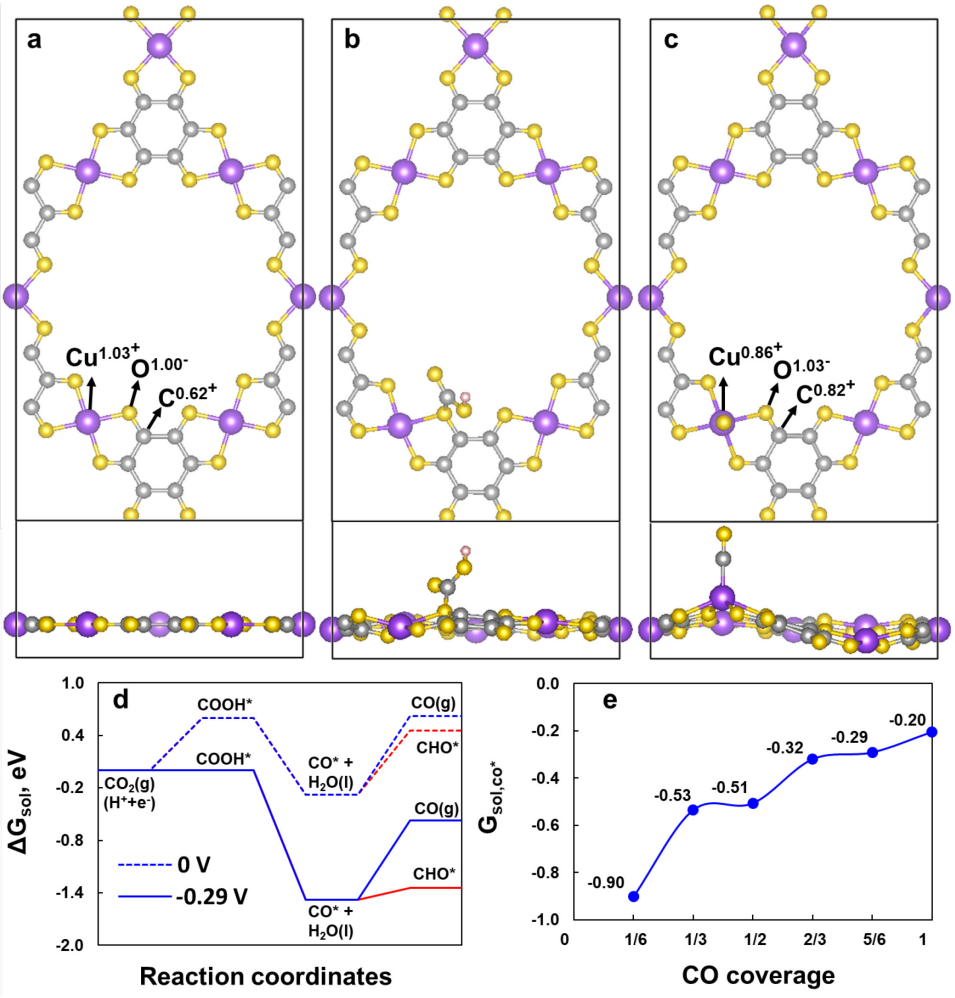

Figure 3. Density Functional Theory Calculations of CO_2RR on Cu-THQ. The top views (upper panels) and side views (bottom panels) of DFT-calculated structures of (**a**) clean Cu-THQ surface (**b**) adsorbed COOH on Cu-THQ surface (**c**) CO molecule (one sixth coverage) on the Cu-THQ surface. The C, O and Cu atoms are depicted in grey, yellow and purple, respectively. Bader charges for Cu, O and C species are shown in (a) and (c). The black lines represent the periodic boundaries. (**d**) The free energies including solvation corrections for CO production on Cu-THQ at 0 V vs RHE in dotted blue lines and at overpotential η of -0.29 V in solid blue lines. The pathways to CHO* are shown with red lines. (**e**) The adsorption free energies of CO at different coverages on Cu-THQ.

Experimental Section

Cathode Preparation: Cu-THQ NFs were synthesized using a liquid-phase exfoliation method. 30 mg of the Cu-THQ powder was dispersed in 12 mL of IPA. Ultra-sonication (Vibra Cell Sonics 130 W) was used for 4-6 hours followed by centrifugation for 60 minutes at 2000-3000 rpm to obtain the corresponding reduced lateral sizes of NFs. For cathode preparation, 200 mg of Cu-THQ NFs was deposited on 1 cm^2 of GDE (Sigracet 25 BC, purchased from FuelCellsEtc). The coated substrate was dried overnight in an argon filled glove box.

DLS Experiments: Malvern Zetasizer Nano ZSP system was used to measure the lateral size of NFs dispersed in IPA at 25 °C. The instrument operates with a 10 mW semiconductor laser with 633 nm emissions.

AFM Experiments: A Bruker ICON Dimension was used to obtain the topography maps of drop-cast flakes and the statistical flake thickness distributions. After drop-casting the Cu-THQ NFs on silicon chips, the substrates were carefully washed by acetone, IPA, and deionized water.

TEM Experiments: Samples for TEM observation were diluted in IPA. A droplet of the suspension was transferred onto a carbon-coated copper grid. High-angle annular dark-field (HAADF) STEM imaging and EDS mapping were performed on a JEOL JEM2100 microscope, and operated at 200 kV (Cs 1.0 mm, point resolution 0.23 nm). TEM images were recorded with a Gatan Ultrascan CCD camera (resolution 2048 x 2048 pixels).

XPS Experiments: A Thermo Scientific ESCALAB 250Xi instrument was utilized to perform XPS experiments. Thermo Avantage software was used to analyze and process each element's data.

Electrolyte Preparation: Choline chloride was ($C_5H_{14}ClNO$) purchased from Sigma-Aldrich. Potassium hydroxide (KOH) was purchased from Fisher-Scientific. The solutions were mixed to the desired concentration using Barnstead NANO pure water (18.2 MΩ and 25 °C).

Electrochemical Experiments: The Cu-THQ coated GDE was used as the working electrode. $Ag/AgNO_3$ (with 0.1 M $AgNO_3$ in 1 M KOH and 1 M choline chloride as filling solution) and platinum mesh (surface area 0.48 cm^2) were used as reference and counter electrodes, respectively. First, CO_2 gas was bubbled for approximately 30 minutes into the electrolyte along with stirring to minimize the mass $_{transfer}$ effect and complete the saturation. The pH of the electrolyte was measured to be ~7.6. LSV experiments were performed in a standard two-compartment electrochemical cell at scan rate of 50 mV s^{-1}. All potentials were converted to RHE (see Supporting Information S7).

DEMS Experiments: Real time analysis of the gas products from CO_2RR was carried out using DEMS (purchased from Hiden Analytical). In order to calibrate the gas species (H_2 and CO), the two compartment cell was used as the working setup and four gas mixtures of 1, 5, 10 and 20 percent for each of the gas species (H_2 and CO) in Argon were chosen. The different gas mixtures were purchased from Praxair. For further details of gas product characterization and DEMS experiments see Supporting Information S8-10.

XANES Experiments: Cu K-edge XANES measurements were conducted between 8867 eV and 9210 eV at beamline 9-BM and longer duration scans were recorded at beamline 10-BM at the Advanced Photon Source. The operando cell was built (Figure S14(a)) with Kapton windows for X-ray passage, with a platinum wire as a counter electrode, $Ag/AgNO_3$ reference electrode, and the Cu-THQ catalyst deposited on GDE was used as a working electrode. The electrolyte was the mixture of 1M choline chloride and 1M KOH. CO_2 gas was bubbled through the electrolyte at a slow rate to induce saturation. Measurements were performed in fluorescence mode using Vortex-ME4 a four-element silicon drift detector. For further details of Cu-L_3 XAS experiments see Supporting Information S16.

DFT Calculations: For details of DFT calculations see Supporting Information S17.

Author contributions

L.M. synthesized the c-MOF NFs and obtained the AFM results. L.M. and S.M. carried out the electrochemical experiments. S.M., A.A. and L.M. performed the DEMS and CO_2RR product analysis. L.M. performed XPS for c-MOF bulk and NFs. L.M. and Z.H. performed DLS. S.R. performed NMR. A.S.K. supervised the electrochemical and characterization experiments. Zh.H. and X.Z. performed the HRTEM and EDS experiment of Cu-THQ NFs. K.K. performed the XAS and operando XANES experiments of Cu-THQ catalyst. J.C. supervised the analysis of XPS, XAS and XANES. N.S., P.Z. and L.C. carried out the computational studies (DFT) of Cu-THQ.

Acknowledgments

The work of A.S.K., L.M., S.M., A.A., S.R. and Z.H. was supported by National Science Foundation DMREF Grant 1729420 and NSF CBET 1800357. The work of K.K. and J.C. was supported by NSF CBET 1800357. N.S., P.Z. and L.C. acknowledge the support from the Office of Science, Basic Energy Sciences, Materials Sciences and Engineering Division. The research at Argonne National Laboratory, a U.S. Department of Energy Office of Science laboratory, operated by UChicago Argonne, LLC was conducted under Contract No. DE-AC02-06CH11357. Use of computational resources from Argonne Laboratory Computing Resource Center is acknowledged. Zh.H and X.Z acknowledge the support by the CATSS project from the Knut and Alice Wallenberg Foundation (KAW 2016.0072), and the Swedish Research Council (VR, 2017-04321, 2016-04625)

We acknowledge Dr. Zhenan Bao and Gan Chen from the Chemical Engineering Department of Stanford University for synthesizing the bulk Cu-THQ c-MOF and performing the corresponding PXRD, SEM and ICP experiments.

References

[1] M. Zhao, Y. Huang, Y. Peng, Z. Huang, Q. Ma, H. Zhang, *Chem. Soc. Rev.* **2018**, *47*, 6267.

[2] H. Bin Wu, X. W. Lou, *Sci. Adv.* **2017**, *3*, 1.

[3] D. Wu, Z. Guo, X. Yin, Q. Pang, B. Tu, L. Zhang, Y. G. Wang, Q. Li, *Adv. Mater.* **2014**, *26*, 3258.

[4] R. Zhao, Z. Liang, R. Zou, Q. Xu, *Joule* **2018**, *2*, 2235.

[5] S. Yuan, L. Feng, K. Wang, J. Pang, M. Bosch, C. Lollar, Y. Sun, J. Qin, X. Yang, P. Zhang, Q. Wang, L. Zou, Y. Zhang, L. Zhang, Y. Fang, J. Li, H. C. Zhou, *Adv. Mater.* **2018**, *30*, 1.

[6] S. Zhao, Y. Wang, J. Dong, C. T. He, H. Yin, P. An, K. Zhao, X. Zhang, C. Gao, L. Zhang, J. Lv, J. Wang, J. Zhang, A. M. Khattak, N. A. Khan, Z. Wei, J. Zhang, S. Liu, H. Zhao, Z. Tang, *Nat. Energy* **2016**, *1*, 1.

[7] X. Deng, R. Li, S. Wu, L. Wang, J. Hu, J. Ma, W. Jiang, N. Zhang, X. Zheng, C. Gao, L. Wang, Q. Zhang, J. Zhu, Y. Xiong, *J. Am. Chem. Soc.* **2019**, *141*, 10924.

[8] C. A. Trickett, A. Helal, B. A. Al-Maythalony, Z. H. Yamani, K. E. Cordova, O. M. Yaghi, *Nat. Rev. Mater.* **2017**, *2*, 1.

[9] H. C. Zhou, J. R. Long, O. M. Yaghi, *Chem. Rev.* **2012**, *112*, 673.

[10] H. Furukawa, K. E. Cordova, M. O'Keeffe, O. M. Yaghi, *Science* **2013**, *341*, 1230444.

[11] D. Nam, O. S. Bushuyev, J. Li, P. De Luna, A. Seifitokaldani, C. Dinh, F. P. García de Arquer, Y. Wang, Z. Liang, A. H. Proppe, C. S. Tan, P. Todorović, O. Shekhah, C. M. Gabardo, J. W. Jo, J. Choi, M. Choi, S. Baek, J. Kim, D. Sinton, S. O. Kelley, M. Eddaoudi, E. H. Sargent, *J. Am. Chem. Soc.* **2018**, *140*, 11378.

[12] E. X. Chen, M. Qiu, Y. F. Zhang, Y. S. Zhu, L. Y. Liu, Y. Y. Sun, X. Bu, J. Zhang, Q.

Lin, *Adv. Mater.* **2018**, *30*, 1.

[13] H. Q. Xu, J. Hu, D. Wang, Z. Li, Q. Zhang, Y. Luo, S. H. Yu, H. L. Jiang, *J. Am. Chem. Soc.* **2015**, *137*, 13440.

[14] M. Ko, L. Mendecki, K. A. Mirica, *Chem. Commun.* **2018**, *54*, 7873.

[15] C. A. Downes, S. C. Marinescu, *ChemSusChem* **2017**, *10*, 4374.

[16] L. Sun, M. G. Campbell, M. Dincə, *Angew. Chemie - Int. Ed.* **2016**, *55*, 3566.

[17] J. Park, A. C. Hinckley, Z. Huang, D. Feng, A. A. Yakovenko, M. Lee, S. Chen, X. Zou, Z. Bao, *J. Am. Chem. Soc.* **2018**, *140*, 14533.

[18] A. J. Clough, J. W. Yoo, M. H. Mecklenburg, S. C. Marinescu, *J. Am. Chem. Soc.* **2015**, *137*, 118.

[19] E. M. Miner, T. Fukushima, D. Sheberla, L. Sun, Y. Surendranath, M. Dincă, *Nat. Commun.* **2016**, *7*, 10942.

[20] H. Jia, Y. Yao, J. Zhao, Y. Gao, Z. Luo, P. Du, *J. Mater. Chem. A* **2018**, *6*, 1188.

[21] D. Feng, T. Lei, M. R. Lukatskaya, J. Park, Z. Huang, M. Lee, L. Shaw, S. Chen, A. A. Yakovenko, A. Kulkarni, J. Xiao, K. Fredrickson, J. B. Tok, X. Zou, Y. Cui, Z. Bao, *Nat. Energy* **2018**, *3*, 30.

[22] D. Sheberla, J. C. Bachman, J. S. Elias, C. Sun, Y. Shao-Horn, M. Dincă, *Nat. Mater.* **2017**, *16*, 220.

[23] M. Asadi, M. H. Motevaselian, A. Moradzadeh, L. Majidi, M. Esmaeilirad, T. V. Sun, C. Liu, R. Bose, P. Abbasi, P. Zapol, A. P. Khodadoust, L. A. Curtiss, N. R. Aluru, A. Salehi-Khojin, *Adv. Energy Mater.* **2019**, *9*, 1.

[24] S. Yu, X. Li, S. Liu, J. Hao, Z. Shao, B. Yi, *RSC Adv.* **2014**, *4*, 3852.

[25] W. Zhu, R. Michalsky, Ö. Metin, H. Lv, S. Guo, C. J. Wright, X. Sun, A. A. Peterson, S. Sun, *J. Am. Chem. Soc.* **2013**, *135*, 16833.

[26] J. Gu, C. S. Hsu, L. Bai, H. M. Chen, X. Hu, *Science* **2019**, *364*, 1091.

[27] N. Han, Y. Wang, L. Ma, J. Wen, J. Li, H. Zheng, K. Nie, X. Wang, F. Zhao, Y. Li, J. Fan, J. Zhong, T. Wu, D. J. Miller, J. Lu, S. T. Lee, Y. Li, *Chem* **2017**, *3*, 652.

[28] X. Zhang, Z. Wu, X. Zhang, L. Li, Y. Li, H. Xu, X. Li, X. Yu, Z. Zhang, Y. Liang, H. Wang, *Nat. Commun.* **2017**, *8*, 1.

[29] N. Morlanés, K. Takanabe, V. Rodionov, *ACS Catal.* **2016**, *6*, 3092.

[30] B. A. Rosen, A. Salehi-Khojin, M. R. Thorson, W. Zhu, D. T. Whipple, P. J. A. Kenis, R. I. Masel, *Science* **2011**, *334*, 643.

[31] Y. Chen, C. W. Li, M. W. Kanan, *J. Am. Chem. Soc.* **2012**, *134*, 19969.

[32] W. Zhu, Y.-J. Zhang, H. Zhang, H. Lv, Q. Li, R. Michalsky, A. A. Peterson, S. Sun, *J. Am. Chem. Soc.* **2014**, *136*, 16132.

[33] Q. Lu, J. Rosen, Y. Zhou, G. S. Hutchings, Y. C. Kimmel, J. G. Chen, F. Jiao, *Nat. Commun.* **2014**, *5*, 3242.

[34] Y. T. Guntern, J. R. Pankhurst, J. Vávra, M. Mensi, V. Mantella, P. Schouwink, R. Buonsanti, *Angew. Chemie Int. Ed.* **2019**, *58*, 12632.

[35] N. Kornienko, Y. Zhao, C. S. Kley, C. Zhu, D. Kim, S. Lin, C. J. Chang, O. M. Yaghi, P. Yang, *J. Am. Chem. Soc.* **2015**, *137*, 14129.

[36] Y. Wang, P. Hou, Z. Wang, P. Kang, *ChemPhysChem* **2017**, *18*, 3142.

[37] I. Hod, M. D. Sampson, P. Deria, C. P. Kubiak, O. K. Farha, J. T. Hupp, *ACS Catal.* **2015**, *5*, 6302.

[38] X. Wang, Z. Chen, X. Zhao, T. Yao, W. Chen, R. You, C. Zhao, G. Wu, J. Wang, W. Huang, J. Yang, X. Hong, S. Wei, Y. Wu, Y. Li, *Angew. Chemie Int. Ed.* **2018**, *57*, 1944.

[39] X. Jiang, H. Wu, S. Chang, R. Si, S. Miao, W. Huang, Y. Li, G. Wang, X. Bao, *J. Mater. Chem. A* **2017**, *5*, 19371.

[40] R. Wang, F. Kapteijn, J. Gascon, *Chem. – An Asian J.* **2019**, *14*, 3452.

[41] Y. Zheng, P. Cheng, J. Xu, J. Han, D. Wang, C. Hao, H. R. Alanagh, C. Long, X. Shi, Z. Tang, *Nanoscale* **2019**, *11*, 4911.

[42] B. X. Dong, S. L. Qian, F. Y. Bu, Y. C. Wu, L. G. Feng, Y. L. Teng, W. L. Liu, Z. W. Li, *ACS Appl. Energy Mater.* **2018**, *1*, 4662.

[43] L. Dai, Q. Qin, P. Wang, X. Zhao, C. Hu, P. Liu, R. Qin, M. Chen, D. Ou, C. Xu, S. Mo, B. Wu, G. Fu, P. Zhang, N. Zheng, *Sci. Adv.* **2017**, *3*, 1.

[44] S. Min, X. Yang, A. Y. Lu, C. C. Tseng, M. N. Hedhili, L. J. Li, K. W. Huang, *Nano Energy* **2016**, *27*, 121.

[45] M. Asadi, K. Kim, C. Liu, A. V. Addepalli, P. Abbasi, P. Yasaei, P. Phillips, A. Behranginia, J. M. Cerrato, R. Haasch, P. Zapol, B. Kumar, R. F. Klie, J. Abiade, L. A. Curtiss, A. Salehi-Khojin, *Science* **2016**, *353*, 467.

[46] P. Abbasi, M. Asadi, C. Liu, S. Sharifi-Asl, B. Sayahpour, A. Behranginia, P. Zapol, R. Shahbazian-Yassar, L. A. Curtiss, A. Salehi-Khojin, *ACS Nano* **2017**, *11*, 453.

[47] NIST X-ray Photoelectron Spectroscopy Database, "NIST Standard Reference Database Number 20," DOI 10.18434/T4T88Kcan be found under https://srdata.nist.gov/xps/, **2000**.

[48] N. S. McIntyre, M. G. Cook, *Anal. Chem.* **1975**, *47*, 2208.

[49] C. Zhu, A. Osherov, M. J. Panzer, *Electrochim. Acta* **2013**, *111*, 771.

[50] M. C. Biesinger, L. W. M. Lau, A. R. Gerson, R. S. C. Smart, *Appl. Surf. Sci.* **2010**, *257*, 887.

[51] P. Gaudin, P. Fioux, S. Dorge, H. Nouali, M. Vierling, E. Fiani, M. Molière, J.-F. Brilhac, J. Patarin, *Fuel Process. Technol.* **2016**, *153*, 129.

[52] T. Böske, K. Maiti, O. Knauff, K. Ruck, M. Golden, G. Krabbes, J. Fink, T. Osafune, N. Motoyama, H. Eisaki, S. Uchida, *Phys. Rev. B - Condens. Matter Mater. Phys.* **1998**, *57*, 138.

[53] R. Sarangi, N. Aboelella, K. Fujisawa, W. B. Tolman, B. Hedman, K. O. Hodgson, E. I. Solomon, *J. Am. Chem. Soc.* **2006**, *128*, 8286.

[54] P. Jiang, D. Prendergast, F. Borondics, S. Porsgaard, L. Giovanetti, E. Pach, J. Newberg, H. Bluhm, F. Besenbacher, M. Salmeron, *J. Chem. Phys.* **2013**, *138*, 024704.

[55] K. Shimizu, H. Maeshima, H. Yoshida, A. Satsuma, T. Hattori, *Phys. Chem. Chem. Phys.* **2001**, *3*, 862.

[56] L. shan Kau, D. J. Spira-solomon, J. E. Spira-solomon-penner-hahn, K. O. Hodgson, E. I. Solomon, *J. Am. Chem. Soc.* **1987**, *109*, 6433.

[57] H. Lim, K. E. Thomas, B. Hedman, K. O. Hodgson, A. Ghosh, E. I. Solomon, *Inorg. Chem.* **2019**, *58*, 6722.

[58] D. Karapinar, N. T. Huan, N. Ranjbar Sahraie, J. Li, D. Wakerley, N. Touati, S. Zanna, D. Taverna, L. H. Galvão Tizei, A. Zitolo, F. Jaouen, V. Mougel, M. Fontecave, *Angew. Chemie - Int. Ed.* **2019**, *58*, 15098.

[59] Z. Weng, Y. Wu, M. Wang, J. Jiang, K. Yang, S. Huo, X. F. Wang, Q. Ma, G. W. Brudvig, V. S. Batista, Y. Liang, Z. Feng, H. Wang, *Nat. Commun.* **2018**, *9*, 1.

[60] A. A. Peterson, F. Abild-Pedersen, F. Studt, J. Rossmeisl, J. K. Nørskov, *Energy Environ. Sci.* **2010**, *3*, 1311.

[61] A. A. Peterson, J. K. Nørskov, *J. Phys. Chem. Lett.* **2012**, *3*, 251.

[62] Y. Hori, A. Murata, R. Takahashi, *J. Chem. Soc. Faraday Trans. 1 Phys. Chem. Condens. Phases* **1989**, *85*, 2309.

[63] W. Tang, E. Sanville, G. Henkelman, *J. Phys. Condens. Matter* **2009**, *21*, 084204.

[64] E. Sanville, S. D. Kenny, R. Smith, G. Henkelman, *J. Comput. Chem.* **2007**, *28*, 899.

[65] G. Henkelman, A. Arnaldsson, H. Jónsson, *Comput. Mater. Sci.* **2006**, *36*, 354.